ELSEVIER

Journal of Electron Spectroscopy and Related Phenomena 117–118 (2001) 153–164

JOURNAL OF ELECTRON SPECTROSCOPY and Related Phenomena

www.elsevier.nl/locate/elspec

Photoemission studies of self-energy effects in cuprate superconductors

P.D. Johnson*, A.V. Fedorov[1], T. Valla

Department of Physics, Brookhaven National Laboratory, Associated Universities Inc., PO Box 5000, Upton, NY 11973-5000, USA

Received 9 October 2000; accepted 29 December 2000

Abstract

Recent instrumentation developments in photoemission are providing new insights into the physics of complex materials. With increased energy and momentum resolution, it has become possible to examine in detail different contributions to the self-energy or inverse lifetime of the photohole created in the photoexcitation process. In studies of a metallic system such as Mo it is possible to isolate and identify the different contributions to the quasi-particle lifetime including electron–electron, electron–phonon and electron–impurity scattering. In contrast, studies of the high T_c superconductor, $Bi_2Sr_2CaCu_2O_{8+\delta}$, show that the material at optimal doping behaves like a non-Fermi liquid rather a Fermi liquid.

Keywords: Photoemission; Superconductivity; Self-energy

1. Introduction

More than a decade after the initial discovery, the exact mechanism responsible for high T_c superconductivity remains a problem at the heart of condensed matter physics and materials science research [1]. Does the mechanism reflect new physics or can it be viewed as a variant on existing theories of superconductivity? Is the decay of excitations in these systems characteristic of a Fermi liquid or is it characteristic of a non-Fermi liquid? Are the properties driven by a phase transition reflecting the presence of a quantum critical point? Among many other experimental techniques, photoemission has made a number of important contributions to these questions. Highlights include the mapping of the Fermi surface [2–4], the identification of d-wave symmetry of the order parameter in the superconducting state [5–7], and the detection of a pseudogap for underdoped compounds above the transition temperature, T_c [8,9].

In any system, electrons (or holes) may interact strongly with the various excitations of that system. Interactions with these excitations, which might include phonons, spin fluctuations and charge density waves amongst others, can modify both the lifetime and the binding energy of the electron. The quantity that describes these effects is the self-energy, $\Sigma(k,\omega)$, the imaginary part of which represents the scattering

*Corresponding author. Tel.: +1-516-282-3705; fax: +1-516-282-2739.

E-mail address: pdj@bnl.gov (P.D. Johnson).

[1]Present address: Department of Physics, University of Colorado, Boulder, CO 80309-0390, USA and Advanced Light Source, Lawrence Berkeley National Laboratory, Berkeley, CA 94720, USA.

0368-2048/01/$ – see front matter
PII: S0368-2048(01)00263-8

rate or inverse lifetime and the real part, the modification to the binding energy. An electron in a solid thus becomes 'dressed' with a 'cloud' of excitations, acquiring a different effective mass, but still behaving as a 'one-particle' excitation or quasiparticle [10]. This represents the traditional Fermi liquid (FL) picture. In more exotic materials, an electron may lose its 'one-particle' integrity and decay completely into collective excitations such as spinons and holons [11].

With the development of new high resolution capabilities in both energy and momentum, photemission has recently been applied to detailed studies of self-energy effects in a number of materials. A measurement of the self-energy allows a determination of the strength of the coupling to excitations or fluctuations and the identification of the energy scale over which the fluctuations occur. As examples, self-energy effects due to the electron–phonon interaction have been identified in metallic systems including molybdenum [12] and beryllium [13,14]. In these cases the energy scale is represented by the Debye energy. More recently self-energy corrections reflecting coupling to fluctuations in the charge density wave order parameter have been observed in the layered dichalcogenide 2H-$TaSe_2$ [15,16]. The extension of such studies to the problem of high T_c superconductivity has offered the possibility of identifying appropriate energy scales describing the fluctuations in these materials [17–19].

2. The photoemission process

The single-particle spectral response $A(\underline{k},\omega) = (-1/\pi)G(\underline{k},\omega)$is given by

$$A(\underline{k},\omega) = \frac{\Sigma''(\underline{k},\omega)}{\left[\omega - \epsilon_k - \Sigma'(\underline{k},\omega)\right]^2 + \left[\Sigma''(\underline{k},\omega)\right]^2} \qquad (1)$$

where $\Sigma'(\underline{k},\omega)$ and $\Sigma''(\underline{k},\omega)$ represent the real and imaginary components of the self-energy, respectively.

Photoemission represents a direct transition between an initial and final state which results in a peak in the excitation spectrum broadened to some width reflecting contributions both from the finite lifetime of the photohole and from the momentum broadening of the photoelectron [20]. The combination results in a total width Γ given by

$$\Gamma = \left(\Gamma_h + \frac{v_h}{v_e}\Gamma_e\right)\left(\left|1 - \frac{v_h}{v_e}\right|\right)^{-1} \qquad (2)$$

where Γ_h is the width of the hole state and Γ_e is the width of the electron state and v_h and v_e are the respective perpendicular velocities. In a two-dimensional system such as the cuprates where $v_h = 0$, the width of the photoemission peak is determined entirely by the width of the photohole, Γ_h and the intensity $I(\underline{k},\omega)$ measured as a result of the photoemission process is given by

$$I(\underline{k},\omega) = |M|^2 A(\underline{k},\omega) f(\omega) \qquad (3)$$

where M represents the matrix element linking initial and final states and $f(\omega)$ is the Fermi function. The latter enters because the photoemission process is restricted to excitation from occupied states below the Fermi level.

The individual components of the self-energy may be obtained either from energy distribution curves (EDCs), the photoemitted intensity as a function of binding energy at constant momentum, or from momentum distribution curves (MDCs), the photoemitted intensity as a function of momentum at constant binding energy [17]. As has been discussed elsewhere, in the vicinity of the Fermi level, the use of MDCs avoids the problems associated with background subtraction and the Fermi distribution cutoff in EDCs [21]. When analyzing MDCs or indeed determining the dispersion in a two-dimensional system the parallel momentum is given by $k_{||} = (2mE/\hbar^2)^{1/2}\sin\theta$, where E is the energy of the photoemitted electron with respect to the vacuum level and θ is the angle of emission.

Considering first a MDC. If the imaginary part of the self-energy is approximately constant over the range of the peak and the dispersion is linear such that $\epsilon_k = v_F^0(k - k_F)$, we find from Eq. (1) that the full width half max (FWHM) is given by $\Delta k = 2|\Sigma''(\omega)|/v_F^0$ where v_F^0 represents the bare or non-interacting velocity. The experimentally measured rate of dispersion or velocity, v_F, is given by

$$v_F = v_F^0[1 - \partial\Sigma'/\partial\omega]^{-1} = v_F^0(1 + \lambda)^{-1} \qquad (4)$$

with λ representing a coupling constant. The FWHM of an EDC, ΔE, on the other hand is given by

$$\Delta E \approx \frac{2|\Sigma''(\omega)|}{1 - \frac{\partial \Sigma'(\omega)}{\partial \omega}} \tag{5}$$

Both EDCs and MDCs can be used for determining dispersions or velocities. However if the self-energy is a strongly varying function of ω, with a significant constant term in its imaginary part, the position of the 'sharp' or coherent component in an EDC will no longer represent the single-particle dispersion. On the other hand, if the self-energy depends only weakly on momentum, the MDCs have a much simpler line-shape, and the peak position will approximately follow the single-particle dispersion. Therefore, velocities deduced from MDCs are more accurate than those extracted from EDCs. However, the finite instrumental resolution will affect such measurements progressively more as the velocities decrease.

2.1. Molybdenum: a Fermi liquid

It has been suggested that the high T_c cuprates represent some form of non-Fermi liquid where the imaginary part of the self-energy takes the form $\mathrm{Im}\,\Sigma = \max(\omega, T)$ [22,23]. This is to be compared with a Fermi liquid where $\mathrm{Im}\,\Sigma = \max(\omega^2, T^2)$ [10]. The quadratic dependence of the latter reflects the exclusion principle in that the decay of any excitation via electron–electron scattering must involve excitations to states outside the Fermi Sea.

Before examining self-energy effects in the superconducting cuprate materials, it is worth reviewing a model Fermi liquid system. In particular, we review the studies of a two-dimensional surface state on the molybdenum(110) surface [12]. The latter represents a suitable analog of the two-dimensional states found in the cuprates because it is also derived primarily from d-orbitals.

In Fig. 1, we show the image of the spectral intensity excited from the surface state or resonance in the $\bar{\Gamma}$–$\bar{N}$ azimuth. In the vicinity of the Fermi level, we note that there is a change in the rate of dispersion or a mass enhancement and a rapid change in the width of the band. The measured

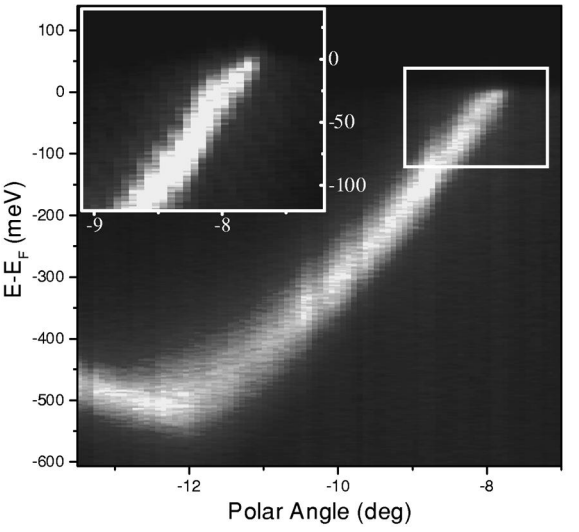

Fig. 1. ARPES intensity plot of the Mo(110) surface recorded along the $\bar{\Gamma}$–$\bar{N}$ line of the surface Brillouin zone at 70 K. Shown in the inset is the spectrum of the region around k_F recorded with particular attention paid to the surface cleanliness.

scattering rate reflects three principal contributions. These include electron–electron, electron–phonon and electron–impurity scattering, all of which add linearly to give the total scattering rate Γ such that

$$\Gamma = \Gamma_{e\text{-}e} + \Gamma_{e\text{-}p} + \Gamma_{imp}. \tag{6}$$

The electron–electron scattering term is given by $\Gamma_{e\text{-}e}(\omega, T) = 2\beta\left[(\pi k_B T)^2 + \omega^2\right]$ where, within the Born approximation, $2\beta = (\pi U^2)/(2W^3)$. Here U represents the on-site Coulomb repulsion and W the bandwidth of the state. The electron–phonon contribution may be calculated via the Eliashberg equation such that [24]

$$\Gamma_{e\text{-}ph}(\omega, T) = 2\pi \int_{\delta}^{\infty} d\upsilon\, \alpha^2 F(\upsilon)\left[2n(\upsilon) + f(\upsilon + \omega) + f(\upsilon - \omega)\right] \tag{7}$$

where $\alpha^2 F$ is the Eliashberg coupling constant and $f(\omega)$ and $n(\omega)$ are the Fermi and Bose-Einstein functions. $\Gamma_{e\text{-}ph}$ increases monotonically with energy up to some cut-off defined by the Debye energy. Above approximately one-third the Debye energy, the temperature dependence of $\Gamma_{e\text{-}ph}(\omega, T)$ is linear

with a slope given by $2\pi\lambda k_B$ where λ is the electron–phonon coupling constant.

Impurity scattering is elastic in that the impurity atoms are considered to have no internal excitations. Thus the scattering rate, Γ_{imp}, is proportional to the impurity concentration, but independent of energy or temperature. In any real system, at sufficiently low temperature, it will be the dominant decay mechanism for a hole close to E_F.

In Fig. 2 we show the measured width of the quasiparticle peak as a function of binding energy. Also shown in the figure is the calculated electron–phonon contribution to the scattering rate using the theoretical α^2F for bulk molybdenum [25]. In the vicinity of the Fermi level the agreement between the calculation and the experimentally measured rapid change in the width is excellent. At binding energies greater than the Debye energy the electron–phonon contribution saturates. Also shown in the figure is a quadratic fit to the measured widths at higher binding energies. The quadratic dependence is an indication that electron–electron scattering plays an important role at these energies. Indeed, the prefactor in the fit is consistent with $U \approx 0.6$ eV as predicted for molybdenum [26] and $W \approx 1.3$ eV, approximately the bandwidth of the surface state. Finally we note that the experimental widths have a binding energy-independent contribution due to scattering from hydrogen impurity centers.

Performing a Kramers-Kronig transform of $\Gamma_{e\text{-}ph}$ one obtains the real part of the self-energy, Σ'. In Fig. 2 this is compared with the change in the dispersion or mass-enhancement observed in the vicinity of the Fermi level. Again, the agreement was found to be excellent.

2.2. The optimally doped cuprate superconductor

2.2.1. The nodal direction

We now consider the cuprate superconductor, optimally doped $Bi_2Sr_2CaCu_2O_{8+\delta}$. In this material the two-dimensional copper-oxygen planes are believed to be the source of the superconducting properties. In that they are two-dimensional they represent excellent systems for photemission studies. In Fig. 3 we show the photemitted spectral intensity

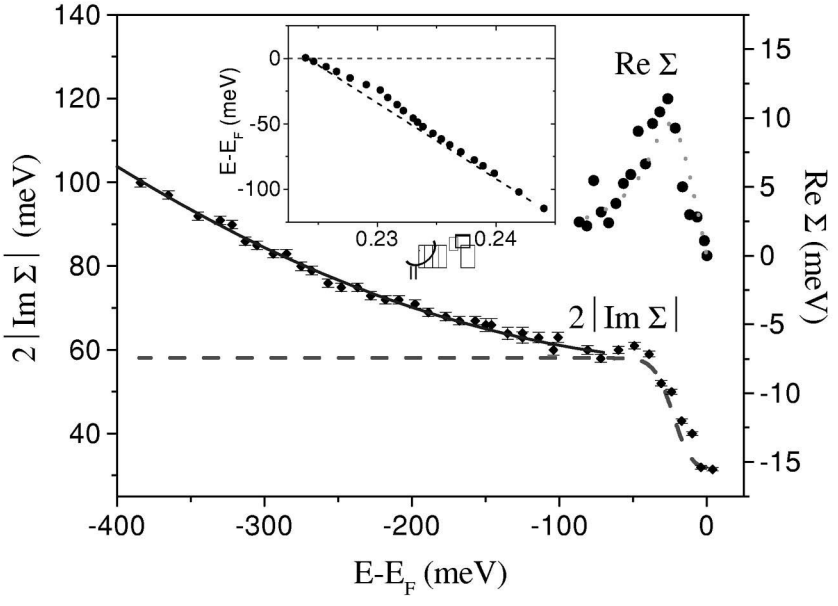

Fig. 2. The photohole self-energy for Mo as a function of binding energy at 70 K. The real part is obtained from the dispersion shown in the inset. The imaginary part is obtained from the width of the quasiparticle peak. The solid line is a quadratic fit to the high-binding energy data ($\omega < -80$ meV). The dashed (dotted) line shows the calculated electron–phonon contribution to the imaginary (real) part of the self-energy. The dashed line is shifted up by 26 meV.

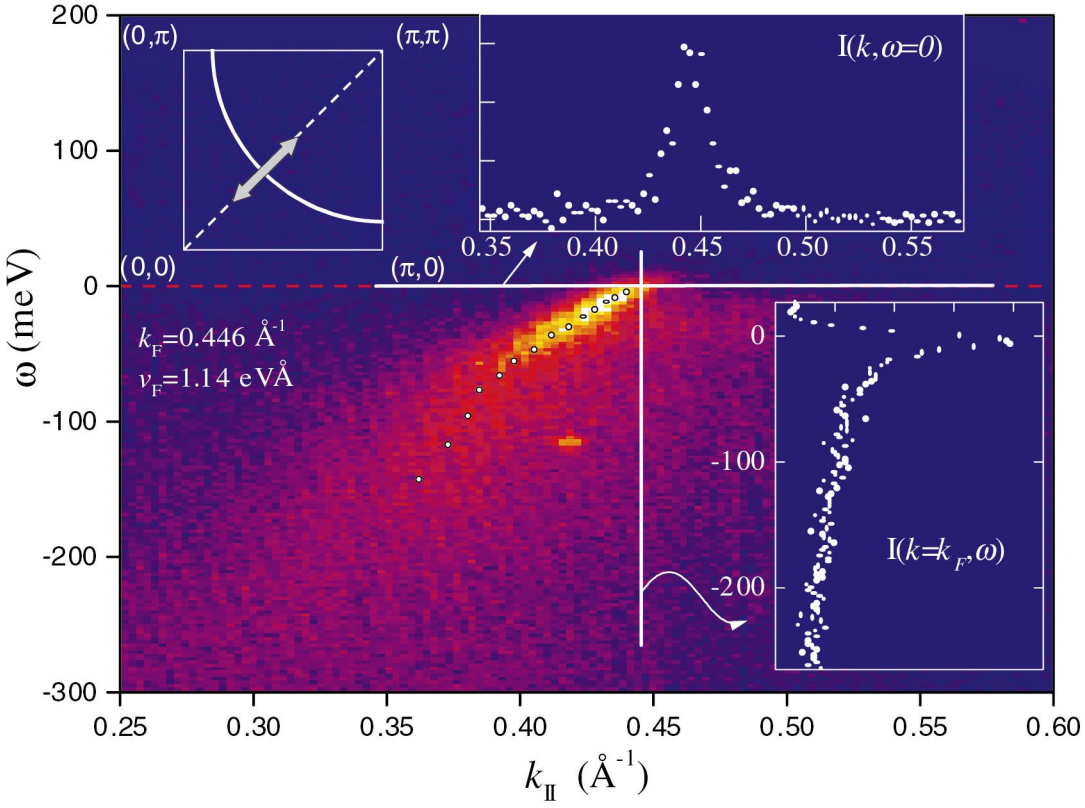

Fig. 3. Two-dimensional spectral plot showing the intensity of emission from optimally doped $Bi_2Sr_2CaCu_2O_{8+\delta}$ in the (π,π) direction of the Brillouin zone as a function ω, the binding energy and $k_{||}$, the parallel momentum. The photon energy is 21.2 eV and the sample temperature is 48 K. Clockwise from upper left the insets show the region of the Brillouin zone sampled in the experiment, a cross-section through the intensity at constant energy ($\omega=0$) as a function of momentum (a MDC), and a cross-section through the intensity at constant angle or momentum ($k=k_F$) as a function of binding energy (an EDC).

measured in the nodal direction, (0,0) to (π,π), as indicated in the inset, when the crystal is in the superconducting state [17]. This particular direction corresponds to a node in the superconducting order parameter and consequently no gap is observable below the transition temperature, T_c.

As discussed earlier, the data may be analyzed using either the EDC or MDC approach as indicated in the figure. In Fig. 4(a), we show the MDCs measured right at the Fermi level, E_F, at different temperatures, both in the normal state and in the superconducting state. In Fig. 4(b) the width of the MDCs, Δk, as a function of temperature are compared with a temperature dependent resistivity curve measured from a sample of the same crystal growth. Both the resistivity $\rho(T)$ and $\Delta k(T)$ show a linear temperature dependence at higher temperatures. Surprisingly, however, the MDC width shows the same linear temperature dependence right through the transition into the superconducting state. This observation suggests that the nodal excitations are unaware of the onset of long-range phase coherence accompanied by the opening of the superconducting gap.

It has been demonstrated elsewhere that the EDCs measured at higher binding energies obey a simple scaling relationship, an indication that Σ'' is linear in binding energy [17]. This latter observation was reported in earlier studies by Olson [27] and has also been confirmed in more recent studies [18,28]. The combined information Σ'', or Im Σ, as a function of binding energy and temperature, determined both

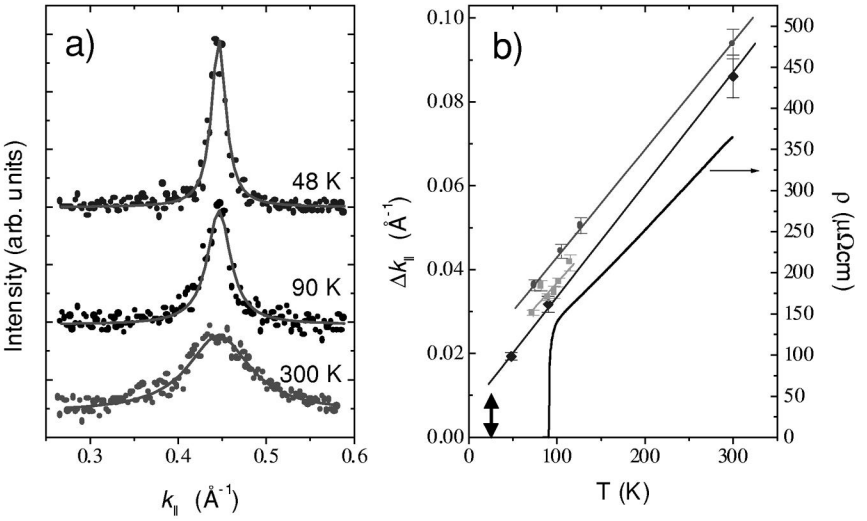

Fig. 4. (a) Momentum distribution curves as a function of temperature. The cuts are made at a binding energy corresponding to the Fermi surface. (b) $\Delta k_{\|}$ obtained from MDCs of the type shown in (a) for three different samples versus temperature. The solid black line shows the temperature dependence of the resistivity ρ measured on an identical sample. The arrow indicates the combined energy and angular contributions to the momentum resolution of the experiment.

from EDCs and MDCs, is shown in Fig. 5. At binding energies, ω, such that $\omega >> \pi T$, Σ'' is linear in ω and at temperatures such that $\pi T >> \omega$, Σ'' is linear in temperature. This behavior, not that of a Fermi liquid was anticipated in early non-Fermi liquid [22] and marginal Fermi liquid models [23] of the normal state of the high temperature superconductors. Not anticipated in those models however, was the observation that the same behavior would persist both above and below the superconducting transition temperature, T_c. In fact as indicated in the inset to the figure, it is possible to scale all of the data so that it falls on a single line for all temperatures. This scaling behavior with an energy/temperature interdependence is very suggestive that the optimally doped material is sitting close to a quantum critical point. In such a system a phase transition driven by some form of quantum fluctuation occurs at zero temperature [29–33]. In fact the MFL model displays quantum critical behavior [34]. More recently Sachdev and coworkers have analyzed a number of different quantum critical scenarios [35,36]. Based on a variety of criteria including the observation of quantum critical scaling in the nodal direction and supporting evidence from teraherz spectroscopy [37], they conclude that the quantum critical point represents a transition between a d-wave superconducting state and a superconducting state with symmetry $d_{x^2-y^2} + id_{xy}$.

If Σ'', the imaginary part of the self-energy, is linear in binding energy, the corresponding real part, Σ', results in a logarithmic correction to the dispersion in the vicinity of the Fermi level. This 'kink' was first reported by Valla et al. in their study of the nodal excitations [17]. In Fig. 6 we show the Σ' for optimally doped $Bi_2Sr_2CaCu_2O_{8+\delta}$, in the normal state obtained by assuming a linearly dispersing non-interacting band passing through k_F and mapping onto the measured dispersion at higher energies. Also shown in the figure is a fit to the data using a simple form for the MFL Σ', $g\omega \log\left(\frac{\omega_c}{x}\right)$ where g represents a coupling constant, ω_c is a UV cut-off and x is given by the max($\omega, \pi T$). Strictly speaking the latter expression is valid only for $\omega, T << \omega_c$. However it is evident that in the normal state the latter provides an excellent description with $\omega_c \sim 230$ meV. It is important to recognize that a 'kink' of this form will exist in any system that has Σ'' linear in binding energy.

In the superconducting state the modification to the dispersion takes a different form [38]. From the doping and temperature dependence it would appear

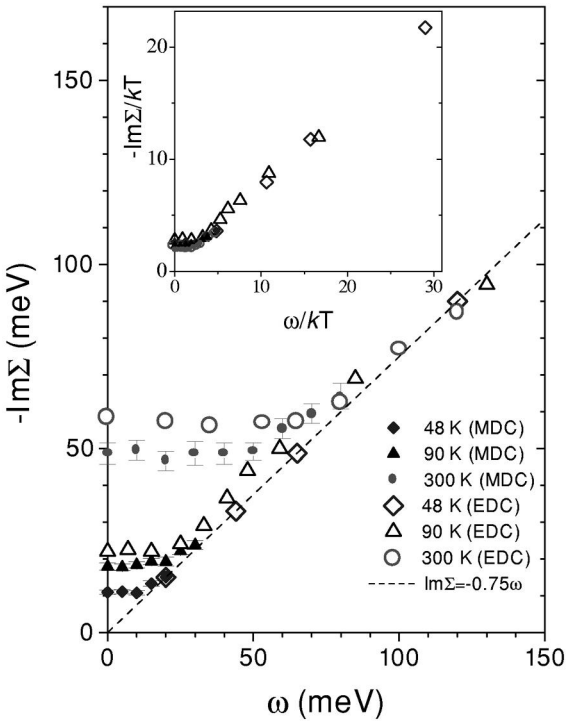

Fig. 5. A compilation of Im Σ obtained via Δk cuts or MDCs and from peak widths in EDCs as a function of binding energy for three different temperatures. The different methods of analysis and different temperatures are indicated. The inset shows the same data plotted in dimensionless units confirming the scaling behavior.

that below T_c the 'kink' reflects coupling to a magnetic resonance mode that is seen in inelastic neutron scattering studies [39,40]. The appearance of an energy scale in the superconducting state as evidenced in the modification to the dispersion should also manifest itself in the imaginary part of the self-energy. As discussed elsewhere [38], the coupling to the mode increases on entering the underdoped region and indeed modifications to the imaginary part of the self-energy are evident in that part of the phase diagram in the superconducting state. However in the optimally doped region the effect appears too subtle to observe unless one moves away from the nodal direction. The observation of an energy scale at the higher energies does not affect the quantum critical scaling at low binding energies.

The non-Fermi liquid models are characterized by a lack of well-defined quasiparticles at the Fermi level. Such well-defined excitations are a necessary condition for defining a Fermi surface. Landau and others have shown that in a Fermi liquid, such well-defined excitations or quasiparticles are characterized by an inverse lifetime or peak width that is smaller than the binding energy of the excitation [41]. In Fig. 7 we compare Σ'' as a function of binding energy for molybdenum and optimally doped $Bi_2Sr_2CaCu_2O_{8+\delta}$. The former has had the constant width resulting from electron–impurity atom scattering subtracted. In the figure the diagonal line represents the boundary between Fermi liquid behavior,

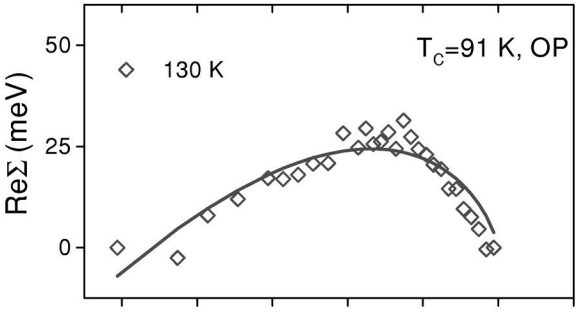

Fig. 6. The real component of the self-energy, Σ', for the optimally doped cuprate determined from the raw data by the procedure described in the text. The solid line represents an MFL fit to the data.

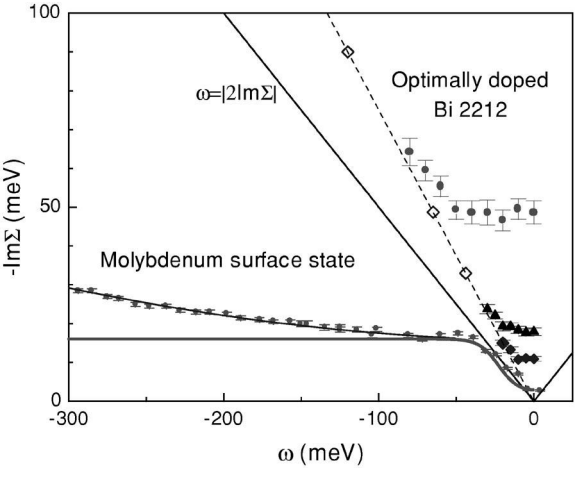

Fig. 7. A comparison of the measured imaginary component of the self-energy, Σ'', for molybdenum and the optimally doped cuprate. The diagonal defines the condition by which $2\Sigma'' = E_b$ where E_b represents the binding energy of the excitation.

such that $2\Sigma''$ or the peak width is less than the binding energy, and non-Fermi liquid behavior. The molybdenum data clearly falls in the former and the high T_c data in the latter.

Another manifestation of the different frequency dependent behavior of Σ'' in the two materials appears in measurements of $n(k)$, the momentum density. For a non-interacting Fermi liquid, $n(k)$ takes the form of a step function at the Fermi wave-vector, k_F. Switching on the interactions results in a rounding of the Fermi surface with a residual discontinuity at k_F proportional to the coherent quasiparticle component. In photoemission studies $n(k)$ is given by

$$n(k) = \int_{-\infty}^{\infty} A(k,\omega) f(\omega)\, \mathrm{d}\omega. \tag{8}$$

In practice the limits of integration are finite reflecting the energy range over which the spectra are acquired. Because at higher energies $\Sigma'' \propto \omega$ for the cuprates and $\propto \omega^2$ for molybdenum, the finite integration range results in very different forms for the measurement as shown in Fig. 8. Note that the two measurements are reversed with respect to each other because the relevant bands disperse in opposite directions in the two materials. The rapid fall off below k_F in the measurement of $n(k)$ for the cuprate has often been mistakenly interpreted as a matrix element effect rather than an insufficient range of integration. In fact the contribution from matrix element effects is indicated by the sloping background.

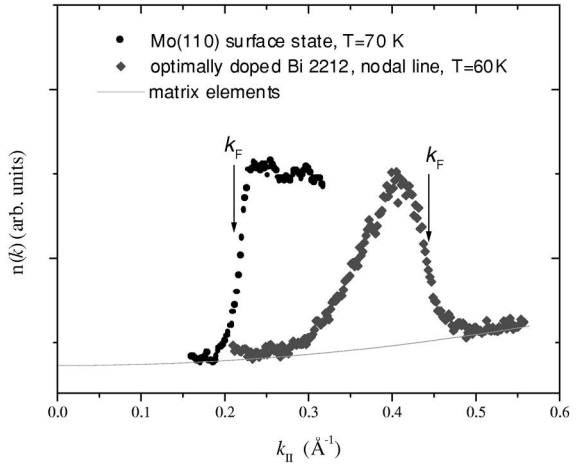

Fig. 8. A comparison of the momentum density for molybdenum and the optimally doped cuprate. The two distributions are reversed with respect to each other because the bands from which they are derived disperse in opposite directions.

2.2.2. Single particle scattering rates and transport measurements

In the previous section we demonstrated that the single-particle scattering rates in the high T_c materials are characteristic of a non-Fermi liquid rather than a Fermi liquid. The scattering rates at the Fermi level in the nodal direction show a linear dependence on temperature in the normal state and this continues through into the superconducting state.

Let us first consider the normal state. The linear temperature dependence of the scattering rate and momentum width in photoemission is reminiscent of the normal state resistivity; linear in T with negligible zero-temperature intersect. As such, it is clearly of interest to determine over what fraction of the Fermi surface the linearity of the momentum spread holds.

In Fig. 9(b), we show the momentum widths determined from MDCs as a function of temperature for different parts of the Fermi surface as indicated in Fig. 9(a) [42]. Note that at E_F the MDCs have a Lorentzian line shape over much of the Fermi surface. It is clear that the linear temperature dependence in the normal state holds over ~70% of the Fermi surface. It is only in the immediate vicinity of the anti-nodal region that the scattering rates show a different temperature dependence. In a simple Drude-type model, the conductivity in a two-dimensional system is proportional to the integral of $k_F l$ over the Fermi surface, where k_F is the Fermi wave vector and $l = 1/\Delta k$ is the mean free path. However, the observation in Fig. 9 that Δk has a negligible zero-temperature offset only along the node, $a(\mathbf{k}_F) \approx 0$, shows that a simple integration would give an incorrect result for resistivity. Indeed the latter would acquire a significant temperature independent term. This means that either the nodal excitations play a special role in the normal state transport, or single-particle scattering rates differ significantly from transport rates. That the normal state transport is dominated by the behavior found in the nodal region,

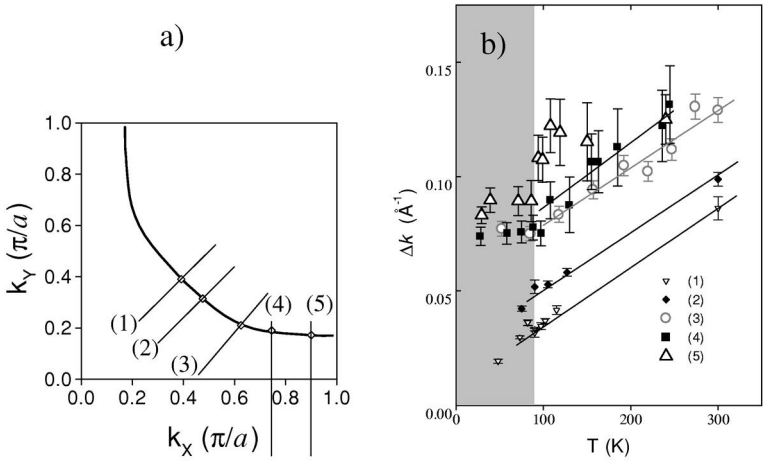

Fig. 9. (a) Fermi surface of the optimally doped $Bi_2Sr_2CaCu_2O_{8+\delta}$, measured in the superconducting state. Indicated are the lines (1) to (5) on which the temperature dependence is measured. (b) Momentum widths (components perpendicular to the Fermi surface) as a function of temperature for different positions on the Fermi surface, obtained by fitting the MDCs with Lorentzian lineshapes. Widths are measured at the Fermi level and at the leading edge, in the normal and in superconducting (gray region) state, respectively.

is not unreasonable if one considers the underlying antiferromagnetic structure of these materials. Along the diagonal or nodal direction, the spins on neighboring copper sites are ferromagnetically aligned. Along the copper oxygen bond direction on the other hand, transport will be frustrated by the antiferromagnetic alignment of the spins on neighboring copper sites. However it is also true that transport discriminates scattering events, emphasizing large momentum transfers (small-angle events do not degrade measured currents). Indeed, thermal transport measurements on $YBa_2Cu_3O_{6+\delta}$ have indicated a sharp increase in the mean free path below T_c [43], a behavior different from that found in the ARPES studies of nodal excitations [17]. When the system enters the superconducting state, the phase space for large momentum transfers collapses and the nodal excitations decay only through the small-angle events. Evidently, the scattering rates measured in thermal transport will be affected by the transition much more than the single-particle scattering rates measured in ARPES.

Abrahams and Varma have suggested that the temperature- and energy-independent term, $a(\mathbf{k}_F)$, represents the scattering on static impurities, placed between the CuO_2 planes [44]. Such impurities would indeed give rise to small-angle scattering, contributing only to single-particle scattering rates and producing a negligible effect on the resistivity. The strong momentum dependence of $a(\mathbf{k}_F)$ is then explained by a variation in the density of states which is available for small-angle scattering at the corresponding momentum. In this picture, the only term relevant for the normal state transport is the temperature- and energy-dependent, but momentum independent marginal Fermi liquid self-energy. More recently in a study of the role of coupling to spin fluctuations, Haslinger et al. have concluded that, contrary to the MFL model, the photoemission data can equally well be fitted with the expression $\Sigma''(k,\omega) = A_k\omega + B$, where the prefactor A_k has a moderate k-dependence and the factor B is constant [45].

Consideration of the anisotropy of the c-axis hopping integral has lead several authors to propose that the anomalous c-axis transport in these materials is dominated by scattering rates in the vicinity of the $(\pi,0)$ point [46–50]. The c-axis resistivity for the optimally doped material is approximately constant over the range from 250 down to 150 K at which point there is an increase in the resistivity before a rapid drop to zero at the transition temperature, T_c [51,52]. The experimental points in Fig. 9(b) corresponding to the $(\pi,0)$ region are consistent with this

temperature dependence. Any integration over the Fermi surface, even if weighted by matrix elements, would give rise to a linear term in the *c*-axis resistivity.

2.2.3. The anti-nodal or (π,0) direction

In Fig. 9(b), we show the continuation of the momentum width measurements through into the superconducting state. The linearity observed in the normal state continues in the vicinity of the node, but away from that region the scattering rates saturate in the superconducting state. This latter observation is consistent with the opening of a gap in the superconducting state in the vicinity of the (π,0) direction. The development of the gap accompanied by the formation of a sharp peak is well documented in the literature [53]. In Fig. 10 we show a measurement of the temperature dependence of these features. The study shows the interesting property that the sharp peak appears in the spectra above T_c and further remains at constant binding energy [53,54]. It also displays an approximately constant width that is independent of temperature and is not resolution limited.

The exact mechanism for the development of the coherent peak below T_c remains an open question. If

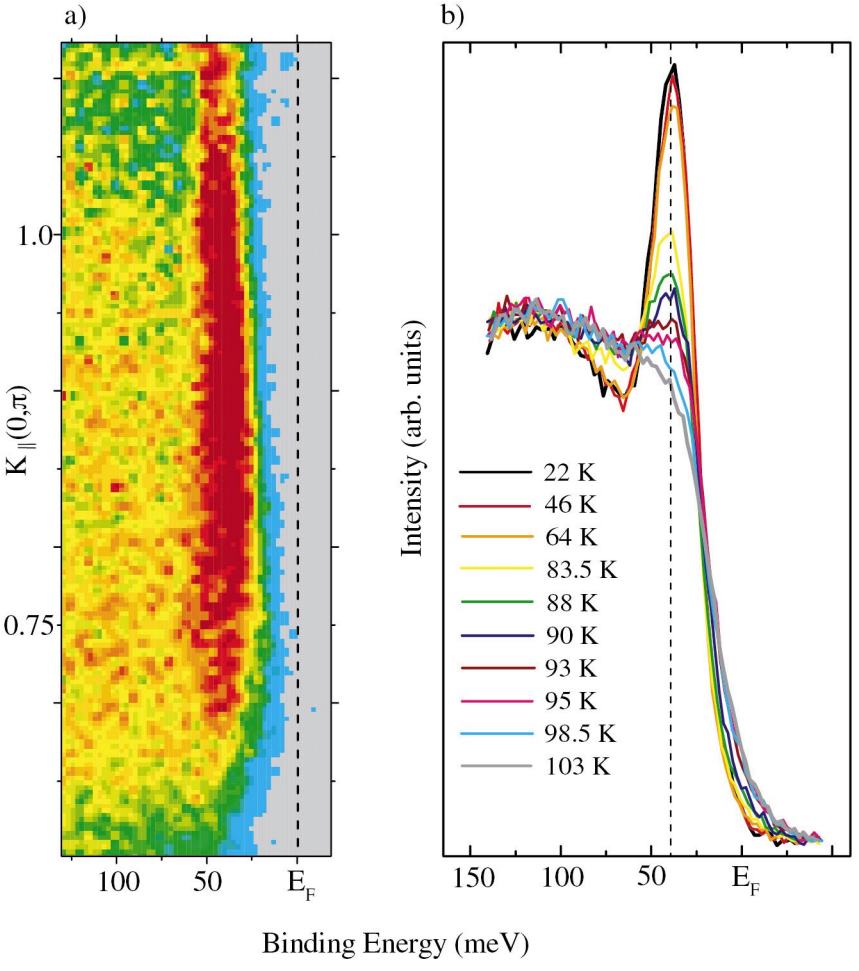

Fig. 10. (a) Spectral density plot recorded from optimally doped $Bi_2Sr_2CaCu_2O_{8+\delta}$ in the ΓM direction with the sample held at 46 K. The incident photon energy is 21.2 eV. The most intense emission is indicated in red. Angle-integrated photemission spectra recorded as a function of temperature and corresponding to the emission along the ΓM line. The different temperatures are indicated.

it represents the formation of paired electrons the observations in Fig. 10 are very different from what we might expect on the basis of BCS theory. In the latter theory the formation of paired electrons and long-range phase coherence occur at the same temperature, T_c. Several models suggest that the peak exists in the superconducting state but disappears in the normal state due to a lifetime catastrophe [55,56]. Still other models view the peak as a form of quasi-electron reflecting a bound spinon–holon pair [57] or the bound state of a spin soliton and a charge soliton [58]. In the latter case the measured gap Δ_0 is given by $\Delta_s + (1/2)\,\Delta_c(T) \sim \Delta_s$ where Δ_s and Δ_c are the spin and charge gaps, respectively.

The magnitude of the gap observed in Fig. 10 is generally taken as a measure of the magnitude of the superconducting gap. In fact close agreement is found between such measurements and the observations of the gap in momentum integrating tunneling studies. However the sharp peak in the (π,0) direction is actually one point on a band that disperses to lower binding energies as one moves towards the Fermi surface as indicated in Fig. 11. Indeed in the vicinity of the Fermi level the dispersion of the band will be of the form $E_k = \left(\epsilon_k^2 + \Delta_0^2\right)^{1/2}$ where ϵ_k is the dispersion in the normal state and again Δ_0 is the superconducting gap. In fact the real gap Δ_0 determined from measurements at the Fermi surface is 24 meV for the optimally doped material.

3. Concluding remarks

Our detailed comparison of the single particle scattering rates in molybdenum and optimally doped $Bi_2Sr_2CaCu_2O_{8+\delta}$ clearly show that the latter presents non-Fermi liquid behavior as opposed to the Fermi liquid behavior of the former. Further our studies indicate that in the nodal direction this behavior appears to continue through into the superconducting state. This latter observation remains controversial [28]. However we note that all photoemission experiments are consistent in that they do not show a dramatic change in the scattering rates at the transition temperature, T_c. Indeed the independent studies appear to show nearly identical temperature dependencies in the scattering rate measured at the Fermi level.

More studies are required to determine the exact decay mechanism of the excitations in these complex materials. Does it represent some variant on electron–electron scattering or does it involve some form

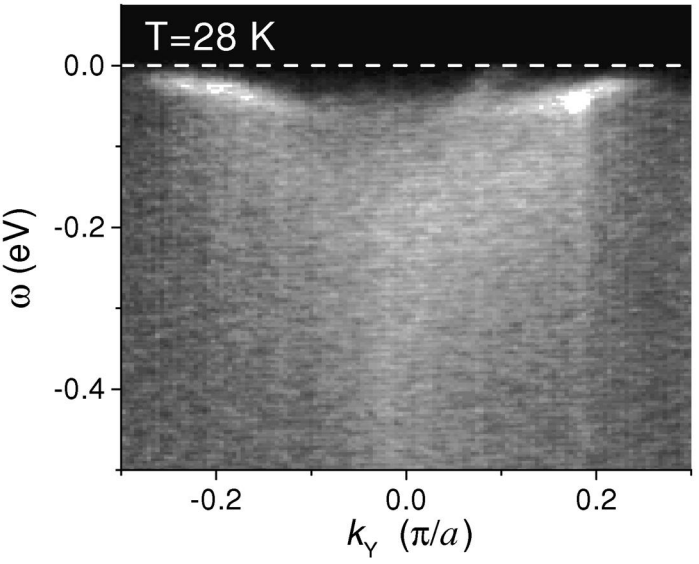

Fig. 11. Spectral intensity recorded from optimally doped $Bi_2Sr_2CaCu_2O_{8+\delta}$ in the superconducting state for a line running orthogonal to the ΓM or (π,0) direction. The line corresponds to line 4 on the Fermi surface map shown in Fig. 9(a).

of spin-charge separation. Does the Fermi liquid behavior discussed here extend into other regions of the phase diagram and what is the exact nature of the quantum critical point. These and many other challenging questions will ensure a continued interest in these materials for some time to come.

Acknowledgements

The authors would like to acknowledge many stimulating discussions with V.J. Emery, J. Tranquada, M. Strongin, D. Basov, B.O. Wells, A. Millis, A. Tsvelik, C.M. Varma, E. Abrahams, G. Sawatzky, S. Sachdev, S. Kivelson, V.N. Muthukumar and many others. The work at Brookhaven National Laboratory is supported by the Department of Energy under contract number DE-AC02-98CH10886.

References

[1] P.W. Anderson, The Theory of Superconductivity in the High-Tc Cuprates, Princeton University Press, Princeton, NJ, 1997.
[2] J.C. Campuzano et al., Phys. Rev. Lett. 64 (1990) 2308.
[3] D.S. Dessau et al., Phys. Rev. Lett. 71 (1993) 2781.
[4] P. Aebi et al., Phys. Rev. Lett. 72 (1994) 2757.
[5] B.O. Wells et al., Phys. Rev. B 46 (1992) 11830.
[6] Z.-X. Shen et al., Phys. Rev. Lett. 70 (1993) 1553.
[7] H. Ding et al., Phys. Rev. B 54 (1996) R9678.
[8] A.G. Loeser et al., Science 273 (1996) 325.
[9] H. Ding et al., Nature 382 (1996) 51.
[10] D. Pines, P. Nozieres, The Theory of Quantum Liquids, Benjamin, New York, 1969.
[11] D. Orgad, S.A. Kivelson, E.W. Carlson, V.J. Emery, X.J. Zhou, Z.X. Shen, cond-mat/0005457 (2000).
[12] T. Valla, A.V. Fedorov, P.D. Johnson, S.L. Hulbert, Phys. Rev. Lett. 83 (1999) 2085.
[13] M. Hengsberger, D. Purdie, P. Segovia, M. Garnier, Y. Baer, Phys. Rev. Lett. 83 (1999) 592.
[14] S. LaShell, E. Jensen, T. Balasubramanian, Phys. Rev. B 61 (2000) 2371.
[15] T. Valla, A.V. Fedorov, P.D. Johnson, J. Xue, K.E. Smith, F.J. DiSalvo, cond-mat/0005477 (2000).
[16] T. Valla, A.V. Fedorov, P.D. Johnson, J. Xue, K.E. Smith, F.J. DiSalvo, Phys. Rev. Lett. 85 (2000) 4759.
[17] T. Valla, A.V. Fedorov, P.D. Johnson, B.O. Wells, S.L. Hulbert, Q. Li, G.D. Gu, N. Koshizuka, Science 285 (1999) 2110.
[18] P.V. Bogdanov et al., cond-mat/0004349 (2000).
[19] A. Kaminski et al., cond-mat/0004482 (2000).
[20] J.E. Inglesfield, E.W. Plummer, in: S.D. Kevan (Ed.), Angle-resolved Photoemission, Elsevier, Amsterdam, 1992.
[21] P.D. Johnson et al., in: P. Pinelta, J. Arthur, S. Brennan (Eds.), Synchrotron Radiation Instrumentation AIP Conference Proceedings No. 521, AIP Press, New York, 2000, p. 73.
[22] P.W. Anderson, in: Proceedings of Fermi International School of Physics, Frontiers and Borderlines in Many-particle Physics, North-Holland, Amsterdam, 1987.
[23] C.M. Varma, P.B. Littlewood, S. Schmitt-Rink, E. Abrahams, A.E. Ruckenstein, Phys. Rev. Lett. 63 (1989) 1936.
[24] G.D. Mahan, Many Particle Physics, Plenum, New York, 1990.
[25] S.Y. Savrason, D.Y. Savrason, Phys. Rev. B 55 (1997) 10895.
[26] W.A. Harrison, Electronic Structure and the Properties of Solids, W.H. Freeman, San Francisco, 1980.
[27] C.G. Olson et al., Phys. Rev. B 42 (1990) 381.
[28] A. Kaminski et al., Phys. Rev. Lett 84 (2000) 1788.
[29] S. Chakravarty, B.I. Halperin, D.R. Nelson, Phys. Rev. B 39 (1989) 2344.
[30] S. Sachdev, J. Ye, Phys. Rev. Lett. 69 (1992) 2411.
[31] A. Sokol, D. Pines, Phys. Rev. Lett. 71 (1993) 2813.
[32] V.J. Emery, S.A. Kivelson, Phys. Rev. Lett. 71 (1993) 3701.
[33] C. Castellani, C. Di Castro, M. Grilli, Phys. Rev. Lett. 75 (1995) 4650.
[34] C.M. Varma, Phys. Rev. B55 (1997) 14554.
[35] S. Sachdev, M. Vojta, cond-mat/0005250 (2000).
[36] M. Vojta, Y. Zhang, S. Sachdev, Phys. Rev. B 62 (2000) 6721.
[37] J. Corson, J. Orenstein, S. Oh, J. O'Donnell, J.N. Eckstein, Phys. Rev. Lett. 85 (2000) 2569.
[38] P.D. Johnson et al., Submitted to PRL.
[39] P. Dai, H.A. Mook, S.M. Hayden, G. Aeppli, T.G. Perring, R.D. Hunt, F. Dogan, cond-mat/0001249 (2000).
[40] H. He, Y. Sidis, P. Bourges, G.D. Gu, A. Ivanov, N. Koshizuka, B. Liang, C.T. Lin, L.P. Regnault, E. Schoenherr, B. Keimer, cond-mat/0002013 (2000).
[41] P.W. Anderson, Basic Notions of Condensed Matter Physics, Benjamin/Cummings, California, 1984, p. 76.
[42] T. Valla, A.V. Fedorov, P.D. Johnson, Q. Li, G.D. Gu, N. Koshizuka, Phys. Rev. Lett. 85 (2000) 828.
[43] N.P. Ong, K. Krishana, Y. Zhang, Z.A. Xu, cond-mat/9904160 (1999).
[44] E. Abrahams, C.M. Varma, Proc. Natl. Acad. Sci. USA 97 (2000) 5714.
[45] R. Haslinger, A.V. Chubukov, Ar. Abanov, cond-mat/0009051 (2000).
[46] S. Chakravarty, A. Sudbo, P.W. Andersen, S. Strong, Science 261 (1993) 337.
[47] O.K. Andersen et al., J. Phys. Chem. Solids 56 (1995) 1573.
[48] L.B. Ioffe, A.J. Millis, Science 285 (1999) 1241.
[49] L.B. Ioffe, A.J. Millis, cond-mat/9908366 (1999).
[50] D. van der Marel, Phys. Rev. B 60 (1999) 6631.
[51] X.H. Chen et al., Phys. Rev. B 58 (1998) 14219.
[52] T. Motohashi et al., Phys. Rev. B 59 (1999) 14080.
[53] A.V. Fedorov et al., Phys. Rev. Lett. 82 (1999) 2179.
[54] A.G. Loeser et al., Phys. Rev. B 56 (1997) 14185.
[55] M. Franz, A.J. Millis, Phys. Rev. B 58 (1998) 14572.
[56] M.R. Norman et al., Phys. Rev. B 57 (1998) R11093.
[57] R.B. Laughlin, Phys. Rev. Lett. 79 (1997) 1726.
[58] E.W. Carlson, D. Orgad, S.A. Kivelson, V.J. Emery, Phys. Rev. B 62 (2000) 3422.